JOURNAL OF GEOPHYSICAL RESEARCH, VOL. 106, NO. D11, PAGES 12,139–12,153, JUNE 16, 2001

Polarized light scattering by inhomogeneous hexagonal monocrystals: Validation with ADEOS-POLDER measurements

Laurent C.-Labonnote, Gérard Brogniez, Jean-Claude Buriez, and Marie Doutriaux-Boucher

Laboratoire d'Optique Atmosphérique, Université des Sciences et Technologies de Lille, Villeneuve d'Ascq, France

Jean-François Gayet

Laboratoire de Météorologie Physique, Université Blaise Pascal, Clermont-Ferrand, France

Andreas Macke

Abteilung Maritime Meteorologie Institut für Meereskunde, Universität zu Kiel, Kiel, Germany

Abstract. Various in situ measurements of the light-scattering diagram in ice clouds were performed with a new nephelometer during several airborne campaigns. These measurements were favorably compared with a theoretical scattering model called Inhomogeneous Hexagonal Monocrystal (IHM) model. This model consists in computing the scattering of light by an ensemble of randomly oriented hexagonal ice crystals containing spherical impurities of soot and air bubbles. It is achieved by using a combination of ray tracing, Mie theory, and Monte Carlo techniques and enables to retrieve the six independent elements of the scattering matrix. This good agreement between nephelometer measurements and IHM model provides an opportunity to use this model in order to analyze ADEOS-POLDER total and polarized reflectance measurements over ice clouds. POLDER uses an original concept to observe ice cloud properties, enabling to measure reflectances and polarized reflectances, for a given scene, under several (up to 14) viewing directions. A first analysis of ice cloud spherical albedoes over the terrestrial globe for November 10, 1996 and April 23, 1997, shows a rather good agreement between measurements and modeling. Moreover, polarized reflectances are also calculated and show a satisfactory agreement with measurements.

1. Introduction

Studies of natural ice clouds are identified as a major unsolved problem in climate research [*Stephens et al.*, 1990] because of the large variability in shape and size of their particles [*Miloshevich and Heymsfield*, 1997]. However, ice clouds are known to have a significant impact on climate [*Liou*, 1986]. Thus to improve our understanding of radiative processes, which strongly depend on microphysical characteristics, we need various in situ and remote radiative measurements of ice clouds. Recently, campaigns such as CIRRUS'98 using an airborne polar nephelometer were held in the south of France to study the optical properties and microphysical characteristics of cloud ice crystals [*Durand et al.*, 1998]. Total and polarized reflectances of ice clouds were measured for 8 months between November 1996 and June 1997 by the POLDER (Polarization and Directionality of Earth's Reflectances) radiometer onboard the Japanese ADEOS platform [*Deschamps et al.*, 1994].

Comparisons with in situ measurements of the differential scattering cross section of cloud particles performed with the airborne polar nephelometer allowed to test the scattering phase functions. These functions are obtained by a theoretical model of light scattering through prismatic ice crystals with air bubble inclusions. This model is called the Inhomogeneous Hexagonal Monocrystals (IHM) model. This theoretical phase function adjusted with in situ measurements was used in order to make a first interpretation of ADEOS-POLDER reflectance measurements over ice clouds [*C.-Labonnote et al.*, 2000].

In this way the purpose of this paper is to investigate the potentialities of the IHM model to interpret ADEOS-POLDER total and polarized reflectance measurements over ice clouds for different days. It also aims at studying the effects of some model parameters on the coefficients of the scattering matrix.

Paper number 2000JD900642.
0148-0227/01/2000JD900642$09.00

2. Modeling

In the approximation of geometrical optics, calculation of the scattering matrix for simple ideal shapes of ice crystals, i.e., Pure Hexagonal Monocrystals (PHM) randomly oriented in space, is commonly obtained by ray-tracing calculations enhanced with Fraunhofer diffraction [*Wendling*, 1979; *Cai and Liou*, 1982; *Takano and Jayaweera*, 1985; *Muinonen*, 1989; *Macke et al.*, 1996a]. These crystals are defined by their length L and radius R, or by the aspect ratio $L/2R$ and the radius R_v of a volume-equivalent spherical particle. Such scattering phase functions have various behaviors chiefly depending on the aspect ratio of the crystals. Following some in situ observations, we have considered a more realistic and coherent

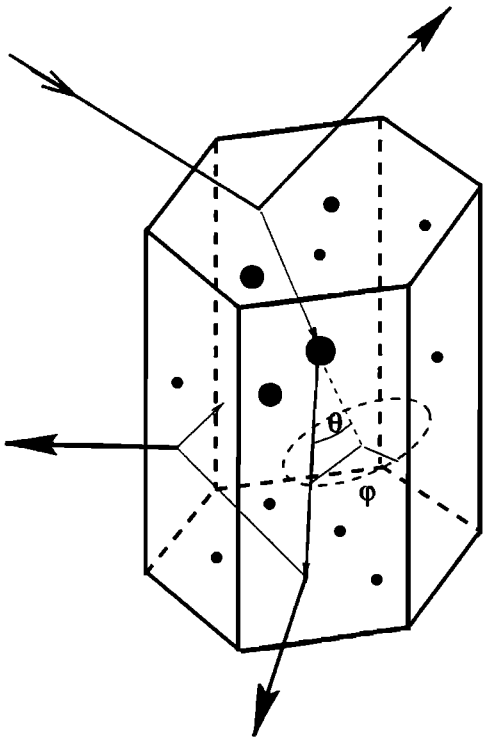

Figure 1. Synoptic scheme of IHM model.

model. Indeed, measurements performed from ice replicator and microphotographic observations [*Strauss et al.*, 1997] have shown that (1) the hexagonal structure of ice particles is rather common due to the natural crystalline structure of ice water at thermodynamical conditions of high-level cirrus clouds. Yet, complicated particles like bullet rosettes, agregates, etc., are often observed in ice clouds. (2) Air bubbles may be trapped inside rapidly growing ice particles or inside suddenly frozen supercooled water droplets [*Hallett*, 1994].

Moreover, measurements performed by the Counterflow Virtual Impactor (CVI) [*Noone et al.*, 1993] have shown that mineral aerosol or soot impurities are sometimes trapped in ice crystals due to the presence of aerosol particles in the upper troposphere serving as ice nuclei, although only a small number (one or two) of impurities per crystal is generally found. To modelize ice cloud particles, we chose to keep the hexagonal structure of randomly oriented ice monocrystals in which we added trapped air bubbles and inclusions of mineral aerosol impurities [*Macke et al.*, 1996b]. We assumed a spherical shape for these impurities (Figure 1). We also assumed that radii of air bubbles or impurities follow a gamma standard law $n(r)$ characterized by the effective radius r_{eff} and the effective variance v_{eff}.

While the ray-tracing technique concerns the refraction and reflection events at the outer boundary of the crystal, the Monte Carlo technique and Mie theory allow to calculate internal scattering events by spherical inclusions. These inclusions are randomly located in the crystal. In this model, two subsequent internal scattering events are characterized by a free path length defined by $\ell = -\langle \ell \rangle \ln([\text{rand}\ell])$ where $\langle \ell \rangle$ is the mean free path length and $[\text{rand}\ell]$ is a random number within the range [0, 1]. In a previous study [*C.-Labonnote et al.*, 2000] the single-scattering phase function of internal scatterers was integrated over the size distribution of inclusions; that is, we used a single-scattering phase function to calculate the new direction of a light ray after an internal scattering event. In this paper we take into account the polarization effect. For that purpose we use the exact radius of each inclusion reached by the photon. Thanks to the size distribution of inclusions, the Monte Carlo method enables us to determine the radius according to

$$N(r) = [\text{rand}n]N(r_{\max}), \tag{1}$$

where

$$N(r) = \int_{r_{\min}}^{r} n(r')\, dr', \tag{2}$$

and $[\text{rand}n]$ is a random number within the range [0, 1]. After an internal scattering event the zenithal direction θ of the scattering of the polarized photon is given by

$$L(\theta) = [\text{rand}\theta]L(\pi), \tag{3}$$

where

$$L(\theta) = \int_0^{\theta} P_{\text{inc}}(\theta') \sin\theta'\, d\theta', \tag{4}$$

$[\text{rand}\theta]$ is a random number within the range [0, 1], and P_{inc} is the scattering phase function of the inclusion calculated from Mie theory for a given radius. Thus we use a set of scattering phase functions to calculate, after an internal scattering event, the new local zenithal angle. Note that this method leads to the same features on the IHM scattering phase function as the nonpolarized method described by *C.-Labonnote et al.* [2000] but is slightly more time consuming for the calculation. Following *Girasole et al.* [1997] and *Rozé* [1999], the azimuthal direction φ of scattering for the zenithal direction θ, is determined according to

$$2\pi[\text{rand}\varphi] = \varphi - \left(\frac{\sin 2\varphi}{2} Q(\theta) + U(\theta) \sin^2\varphi\right) S(\theta), \tag{5}$$

where

$$S(\theta) = \frac{|S_1(\theta)|^2 - |S_2(\theta)|^2}{|S_1(\theta)|^2 + |S_2(\theta)|^2}, \tag{6}$$

and $[\text{rand}\varphi]$ is a random number within the range [0, 1]. This equation depends on the two Stokes parameters $Q(\theta)$ and $U(\theta)$ of the incident polarized light upon the inclusion. The coefficients $S_1(\theta)$ and $S_2(\theta)$ [*van de Hulst*, 1981] of the amplitude matrix are calculated by using Mie theory for the zenithal direction θ of scattering. We can notice from (5) that $2\pi[\text{rand}\varphi] = \varphi$ is the probability to find φ when the polarization is not considered. The amplitude matrix also allows to obtain the two parallel and perpendicular components of the scattered electric field with respect to the local scattering plane.

To treat inclusions as independent scatterers and to assure the validity of Snell-Descartes law and Fresnel formulas, we assumed that the minimum distance between two subsequent events is larger than 4 times the particle radius [*Mishchenko et al.*, 1995]. The percentage p of mineral aerosols with respect to air bubble populations is introduced. The absorption is taken into account by multiplying the energy of the photon with the

Table 1. Physical Characteristics of the Model

N	82 l^{-1} (Midlevel) 225 l^{-1} (Top level)
$L/2R$	220 μm/44 μm
R_v	40 μm
$\langle \ell \rangle$	15 μm
$r_{\text{eff}} - v_{\text{eff}}$	1.0 μm – 0.1
C_{sca}	15450 μm^2

single-scattering albedo of the inclusion. This process is repeated until the photon hits the crystal boundary where it can be reflected or it can exit, following Fresnel's laws. Thus we can follow the trajectory of a photon until its energy falls below 10^{-5} times the energy of the incident photon.

Studying the effect of the presence of impurities in the crystal, we notice that one or two soot inclusions have a negligible effect on scattering; so we choose in this paper the value of the percentage p equal to zero (100% air bubbles). Consequently, the single-scattering albedo value is nearly equal to unity in the visible range. Finally, optical properties of the IHM model are mainly characterized by the four following structural parameters: (1) the aspect ratio $L/2R$ of the crystal, (2) the mean free path length of the light $\langle \ell \rangle$ between two inclusions, (3) the effective radius of the gamma standard size distribution of inclusions r_{eff}, and (4) the effective variance of the gamma standard size distribution of inclusions v_{eff}. Among the elements of the scattering matrix, the most important ones governing the total and polarized radiances, are the scattering phase function P_{11} and the degree of linear polarization $-P_{12}/P_{11}$. Thus we limit our study to the effects of the four above mentioned structural parameters on P_{11} and $-P_{12}/P_{11}$. For this purpose we fix the key value of three parameters, allowing the fourth to vary. The parameters vary around the key values summarized in Table 1.

2.1. Effect of Structural Parameters on the IHM Scattering Phase Function

The effect of structural parameters on the IHM scattering phase function is presented in Figure 2. For a pure ice crystal, varying the equivalent-sphere radius R_v does not affect the scattering properties of the crystal in the visible range, except for the diffraction peak. On the contrary, when a crystal has impurities, changing the equivalent-sphere radius while keeping $\langle \ell \rangle$ constant makes the scattering properties of the crystal change. *Mishchenko and Macke* [1997] have characterized the total amount of inclusions by their optical thickness rather than by $\langle \ell \rangle$. Then, the variation of R_v for a given optical thickness does not change the scattering properties of the particle. If we consider R_v values within the range 30–50 μm, the variation on asymmetry parameter g is very low and does not affect the subsequent study. Thus we fix a realistic mean value of R_v to 40 μm [*Heymsfield et al.*, 1990; *Gayet et al.*, 1996].

The aspect ratio $L/2R$ affects the scattering properties of the crystal through the magnitude of the haloes. Indeed, the 46° halo magnitude increases when $L/2R$ decreases, whereas the 22° halo magnitude increases when $L/2R$ increases (Figure 2a). Note that $L/2R = 1$; i.e., the most compact shape, gives the smaller value of the asymmetry parameter g, as for PHM model [*Chepfer et al.*, 1998].

For a given crystal shape and a given size distribution of impurities the decreasing of $\langle \ell \rangle$ provides a noticeable broadening of the scattering features, as well as a strong decreasing of the 22° and 46° halo magnitudes. Indeed, the decreasing of $\langle \ell \rangle$ leads to smooth the scattering phase function and decreases the asymmetry parameter g (Figure 2b). Such a smoothing effect on the phase function produced by a large number of inclusions has already been described for hexagonal particles [*Macke et al.*, 1996b] and for other host particles like spheres [*Mishchenko and Macke*, 1997]. Other mechanisms like roughness of crystal facets can also smooth the phase function [*Yang and Liou*, 1998; *Knap et al.*, 1999].

For given values of $L/2R$, $\langle \ell \rangle$, and v_{eff}, forward scattering and effective radius vary in the same way, whereas backward scattering varies in the opposite way. Consequently g and r_{eff} increase together (Figure 2c). This behavior is due to a stronger diffraction effect as the size of inclusions increases.

Finally, for a given value of $L/2R$, $\langle \ell \rangle$, and r_{eff}, Figure 2d shows that forward scattering diminishes, whereas side and backward scattering grows along with v_{eff}. Indeed, a high value of v_{eff} induces small inclusions that scatter light more isotropically than large inclusions and thus decreases g.

2.2. Effect of Structural Parameters on the Degree of Linear Polarization

The effect of structural parameters on the degree of linear polarization is presented in Figure 3. Figure 3a presents the influence of the aspect ratio $L/2R$ for fixed key values of $\langle \ell \rangle$, r_{eff}, and v_{eff}. From the most compact shape of the crystal, i.e., a value of $L/2R = 1$, an increase or a decrease of $L/2R$ statistically leads to a decrease of the number of internal reflections and, consequently, to an increase of polarized light. Figure 3b presents the influence of $\langle \ell \rangle$ for fixed values of $L/2R$, r_{eff}, and v_{eff}. Increasing the number of inclusions, i.e., decreasing $\langle \ell \rangle$, leads to depolarize the light. Indeed, when $\langle \ell \rangle$ increases (from 15 to 60 μm), the value of $-P_{12}/P_{11}$ increases, especially in the range [90°–150°], until it reaches the value obtained for a pure ice crystal. Figure 3c presents the influence of the effective radius r_{eff} of inclusions for fixed values of $L/2R$, $\langle \ell \rangle$, and v_{eff}. As r_{eff} increases (from 0.5 to 2 μm), the maximum of the degree of linear polarization decreases due to Mie scattering properties: as the inclusion radius grows, the light polarization diminishes.

Finally, Figure 3d presents the influence of the effective variance v_{eff} for fixed values of $L/2R$, $\langle \ell \rangle$, and r_{eff}. As v_{eff} increases (from 0.02 to 0.3), the degree of linear polarization increases, still due to the size of inclusions. Indeed, a high value of v_{eff} induces small inclusions, which further polarizes the light.

Considering these effects, the previous structural parameters allow to adjust the IHM model with the measurements. For example, in the studied ranges, the minimum of the degree of linear polarization is obtained with the following set: $L/2R = 1$, $\langle \ell \rangle = 15$ μm, $r_{\text{eff}} = 2$ μm, and $v_{\text{eff}} = 0.02$.

Figure 4 presents a comparison of the six independent elements of the scattering matrix from the IHM and PHM models for randomly oriented hexagonal monocrystals. Crystals have an aspect ratio $L/2R = 5$ and a radius of a volume-equivalent spherical particle $R_v = 40$ μm. The PHM model is compared to IHM, which is characterized by a mean free path length $\langle \ell \rangle = 15$ μm, an effective radius of inclusions $r_{\text{eff}} = 1$ μm (which are only air bubbles), and an effective variance $v_{\text{eff}} = 0.1$.

According to *Lacis and Mishchenko* [1995], we can determine the density of inclusions N_t which is described by the volume extinction coefficient $\beta = 1/\langle \ell \rangle$. The density of the

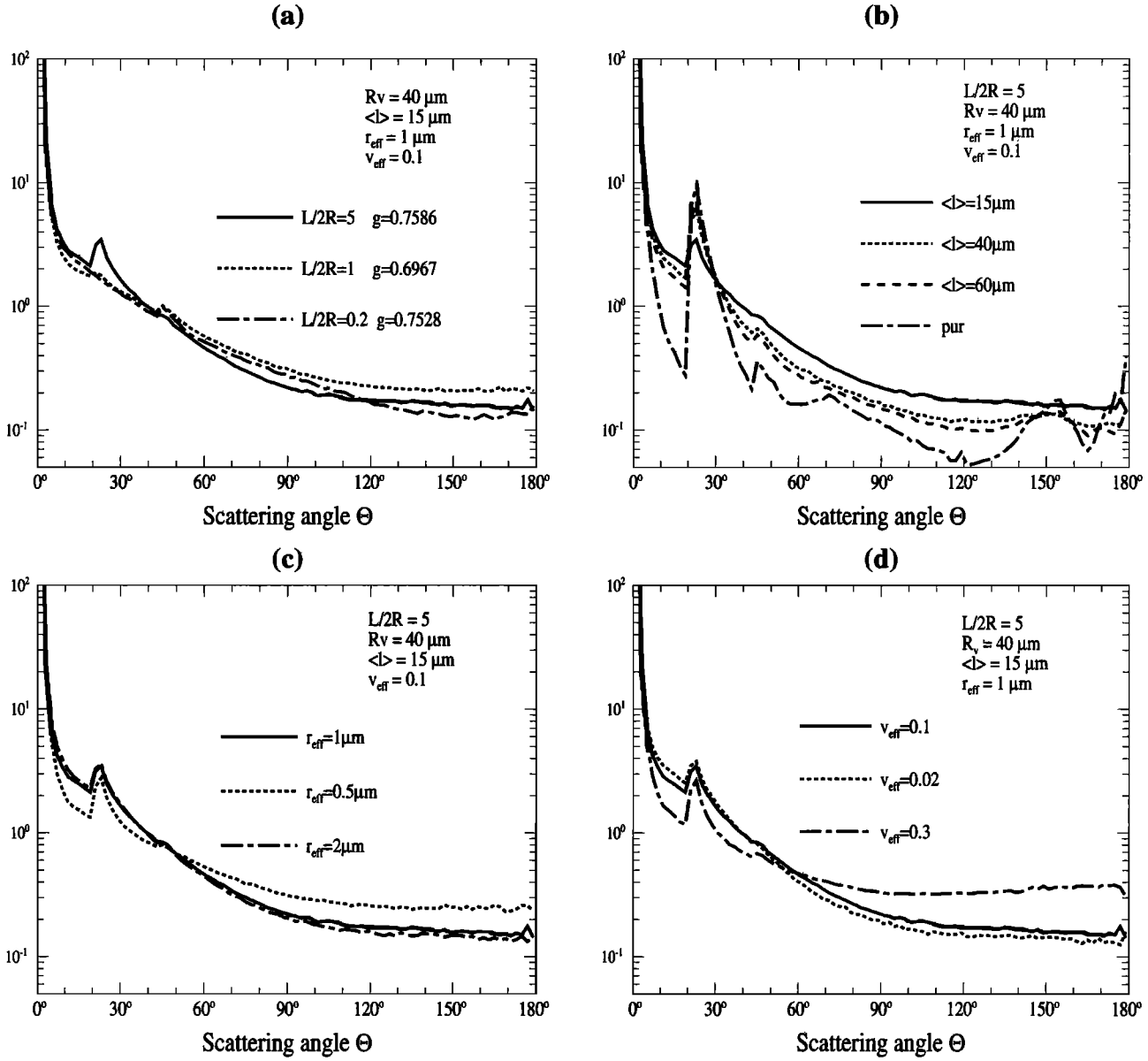

Figure 2. Effects of aspect ratio, mean free path length, and parameters of the gamma standard law of inclusions on the phase function for particles randomly oriented in space.

inclusions, the size of which follows a gamma standard distribution, is given by

$$N_i = \frac{\beta}{\pi r_{\text{eff}}^2 (1 - v_{\text{eff}})(1 - 2v_{\text{eff}}) Q_{\text{ext}}}, \tag{7}$$

where Q_{ext} is the extinction efficiency of inclusions. The above mentioned structural parameters correspond to a value of the inclusions density $N_i \simeq 1.5 \times 10^{-2}$ μm^{-3}, which leads to about 4000 inclusions per crystal, i.e., a relative volume concentration of ≈6%. There are no experimental proofs for this value, but it seems to be reasonably realistic. The coefficients of the scattering matrix obtained with the IHM model have a very smooth behavior according to scattering angle and give results rather comparable to those obtained with complex-shaped models [*Macke et al.*, 1996a].

Note that the values of the elements P_{12}/P_{11} and P_{34}/P_{11}, for symmetry reasons, has to be equal to zero in the backscattering direction ($\Theta = 180°$), and P_{22}/P_{11} cannot be negative [*Mishchenko and Hovenier*, 1995]. In fact, ray-tracing calculations do not allow to obtain a result at a given scattering angle but only in a box around this scattering angle. That is why the values of these three elements in the last box ($\Theta = [179°, 180°]$) can differ from the expected value at $\Theta = 180°$.

3. Airborne Polar Nephelometer

The prototype of the polar nephelometer and its airborne version has already been described in detail [*Crépel et al.*, 1997; *Gayet et al.*, 1997]. The airborne polar nephelometer probe is designed to measure the optical and microphysical parameters of ice or liquid water clouds containing spherical droplets, prismatic crystals, or a mixture of these two components, over a mean size range from a few micrometers to about 500 μm. Figure 5 shows the pattern of the instrument. The basic prin-

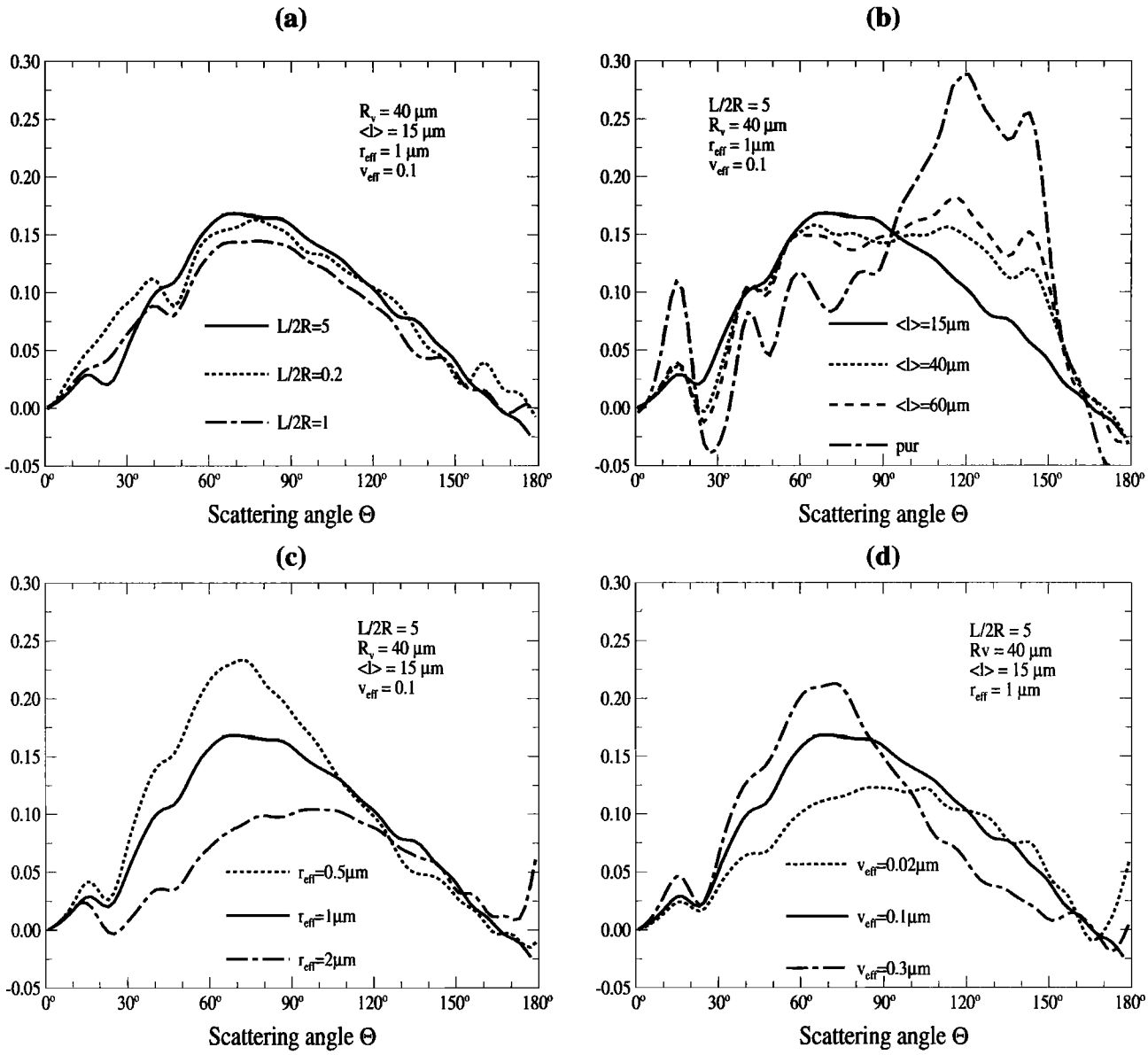

Figure 3. Effects of aspect ratio, mean free path length, and parameters of the gamma standard law of inclusions on the degree of linear polarization for particles randomly oriented in space.

ciple consists in measurements of the differential scattering cross-section $\sigma^d_{sca}(\Theta)$ of light scattered by cloud particles. Because of the optical design, the scattering angles are sampled from 3.5° to 169° by a circular array of 54 photodiodes. The unpolarized incident light is provided by a high-power laser diode at 804 nm.

Several airborne experiments using the polar nephelometer have already been achieved [*Gayet et al.*, 1998], but because of their high level, few in situ studies of ice clouds have been performed with this instrument so far. Among them, CIRRUS'98 was an aircraft experiment performed from January 15 to February 20, 1998, in southeastern France in an area located between longitudes −0.5° and 1.5° and between latitudes 44.6° and 45.3° [*Durand et al.*, 1998]. The polar nephelometer was installed onboard the aircraft TBM 700 flying at a ceiling altitude of about 11,000 m.

Figure 6 shows examples of measurements performed from polar nephelometer and PMS OAP-2D2-C probe. Figure 6 (top) presents measurements of the differential scattering cross section $\sigma^d_{sca}(\Theta)$ as a function of scattering angle Θ, for two different cirrus clouds observed on February 16 at the altitude of 7700 m (midlevel in the cloud) and on February 19 at the altitude of 10,500 m (uppermost level in the cloud). These measurements show different scattering properties due to different microphysical characteristics of cirrus clouds. There are evidenced by the particle size distribution measurements (Figure 6 (bottom)) directly obtained from the PMS OAP-2D2-C probe installed onboard the aircraft. Indeed, the midlevel distribution sampling gives an effective size S_{eff} of the crystal distribution of about 100 µm with a total crystal concentration N of about 75 particles per liter; for the other sampling we have obtained $S_{eff} \simeq 175$ µm and $N \simeq 50$ particles per liter. Otherwise, measurements of the differential scattering cross section are relatively smooth. They sometimes show weak peaks corresponding to 22° and 46° haloes (Figure 6 (top)), which demonstrate the presence of ice crystals with a

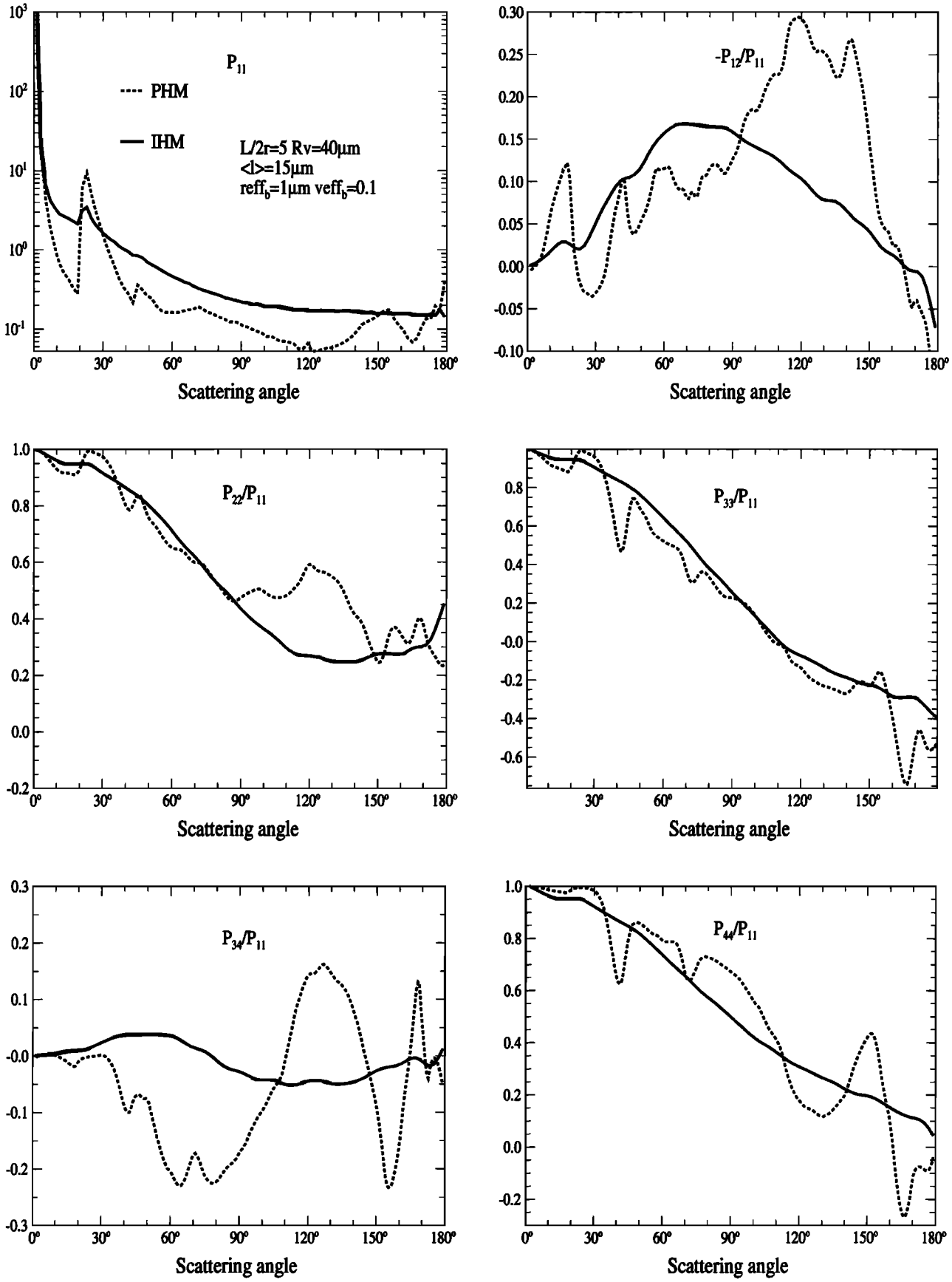

Figure 4. Coefficient of the scattering matrix as a function of scattering angle for ensembles of IHM and PHM particles randomly oriented in space. These two models of crystals have the same aspect ratio and radius of a volume-equivalent sphere ($L/2R = 5$, $R_v = 40$ μm).

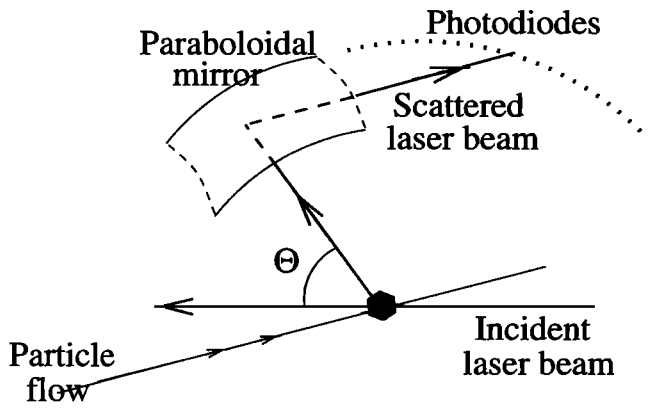

Figure 5. Synoptic scheme of the polar nephelometer.

hexagonal basic structure. We have adjusted our IHM model to nephelometer measurements following the relationship

$$P(\Theta) = \frac{4\pi}{NC_{sca}} \sigma^{d}_{sca}(\Theta), \quad (8)$$

where N is the total particle concentration, C_{sca} is the mean scattering cross section for the randomly oriented particle, and $P(\Theta)$, the normalized scattering phase function [*C.-Labonnote et al.*, 2000]. This adjustment takes into account (1) the size and the concentration of the IHM particles, which are directly related to the value of the product NC_{sca} and which are strongly linked to the magnitude of the measurements; (2) the aspect ratio $L/2R$, which governs the relative magnitude of the secondary scattering peaks at $\Theta = 22°$, and 46°; and (3) the mean free path length $\langle \ell \rangle$ which is linked to the side scattering feature. Thus we have a set of parameters to retrieve nephelometer measurements. It appears obvious that the solution is not unique. Considering the uncertainties, the chosen parameter values, summarized in Table 1, are in agreement with in situ probe measurements in cirrus clouds and seem to be the most realistic choice.

4. POLDER

POLDER (Polarization and Directionality of Earth's Reflectances) uses an original concept to observe a given scene in various spectral channels in the shortwave range and under various observation angles thanks to a rotating filter wheel and a CCD matrix. Moreover, some channels have polarization capabilities. In particular, total and polarized reflectances measured under various scattering angles led to define microphysical properties of ice cloud particles during the airborne experiment EUCREX'94 (European Cloud Radiation Experiment) [*Sauvage et al.*, 1999; *Chepfer et al.*, 1999]. The spaceborne version of POLDER onboard the Japanese polar orbiting platform ADEOS-1 worked for 8 months from November 1996 to June 1997. Some information about POLDER observations of ice clouds are reported in Figure 7 for November 10, 1996 and April 23, 1997. Figure 7a shows the histogram of ice cloud events as a function of the latitude. The distribution of observed ice clouds with respect to the latitude varies with the season. Figure 7b shows the histogram of the solar zenith angle corresponding to the ice cloud observations, and Figure 7c is the histogram of the observed optical thicknesses. This histogram is rather similar for the two days, because all types of ice clouds were observed by POLDER over one day (14 overpasses).

4.1. Spherical Albedo

Measurements of bidirectional reflectances obtained from the POLDER instrument are used to retrieve the visible cloud optical thickness at 670 nm [*Buriez et al.*, 1997]. Here the optical thickness is expressed equivalently in terms of cloud spherical albedo (assuming a black underlying surface). The original POLDER retrieval used a discrete-ordinates method [*Stamnes et al.*, 1988] to compute the cloud spherical albedo without distinction between liquid (assumed spherical) and solid (assumed nonspherical) particles, although this distinction can be made from polarization measurements [*Parol et al.*, 1999]. Specifically, for ice cloud scenes we reprocessed the POLDER data for November 10, 1996 and April 23, 1997, using three models: (1) the IHM model, whose parameters are in agreement with nephelometer measurements (see Table 1), (2) the PHM model, whose external sizes correspond to those of the IHM model (PHM_5), and (3) the PHM model with

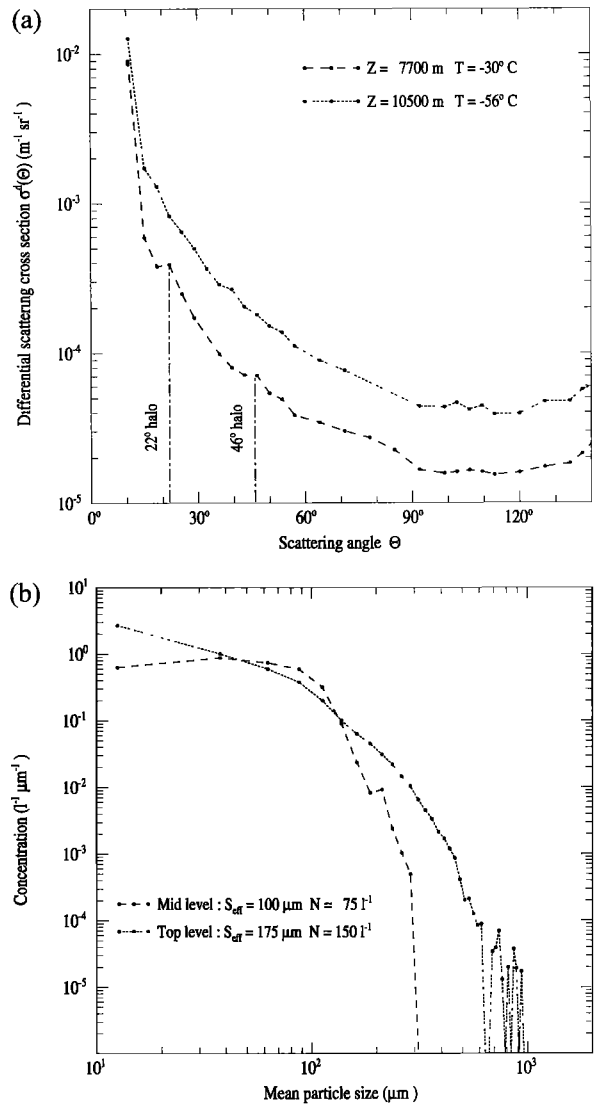

Figure 6. (top) Polar nephelometer measurements and (bottom) corresponding particle size distribution from PMS OAP-2D2-C probe.

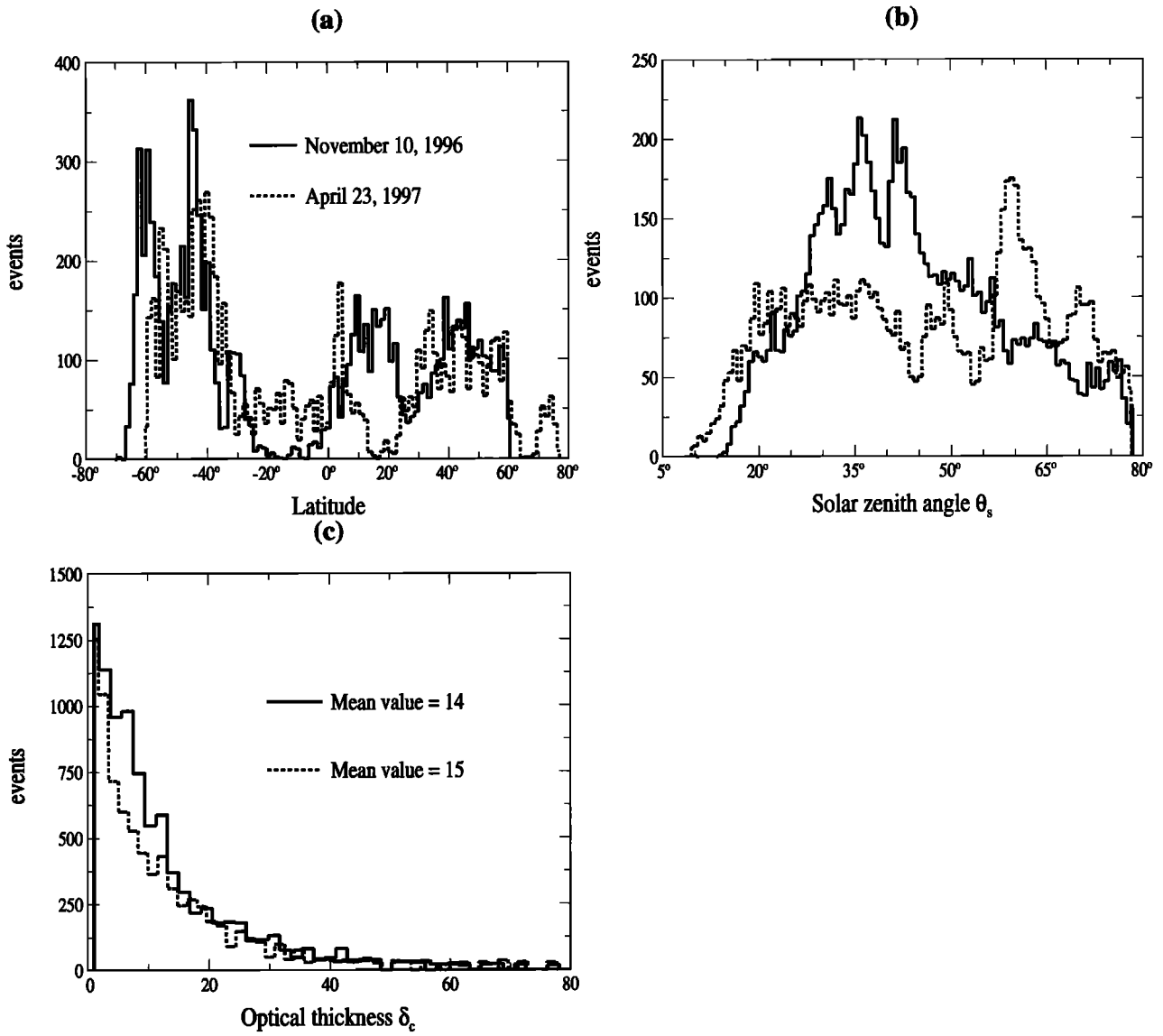

Figure 7. Information about POLDER measurements.

aspect ratio $L/2R = 0.05$ ($PHM_{0.05}$) which was convenient for the case study of EUCREX'94 [*Chepfer et al.*, 1998]. We selected a subset of pixels over ocean by applying the following criteria: 100% ice cloud cover, absence of sea ice, a minimum of seven directions available for observation, and a difference between maximum and minimum scattering angles of at least 50° [*Doutriaux-Boucher et al.*, 2000]. Unfortunately, because of these criteria on scattering angles and the geometry of the optical design of POLDER, most of these pixels were located in midlatitude areas.

POLDER allows to observe a geographic target under up to 14 viewing directions, each corresponding to a different scattering angle (Figure 8). For a given cloudy pixel the cloud spherical albedo is retrieved for each of these N ($7 \leq N \leq 14$) viewing directions. Plate 1 shows the difference between "directional" values of the cloud spherical albedo and the average value over all available directions as a function of the scattering angle for data corresponding to November 10, 1996 and April 23, 1997. These scatterplots were obtained with up to 60,000 points. Plates 1a, 1b, and 1c correspond to IHM, PHM_5, and $PHM_{0.05}$ models, respectively. Note that the same behavior is obtained for the two considered periods. It clearly appears that the IHM scattering phase function model is very appropriate to interpret radiative properties of ice clouds. For IHM, standard deviations of the residual directional albedoes

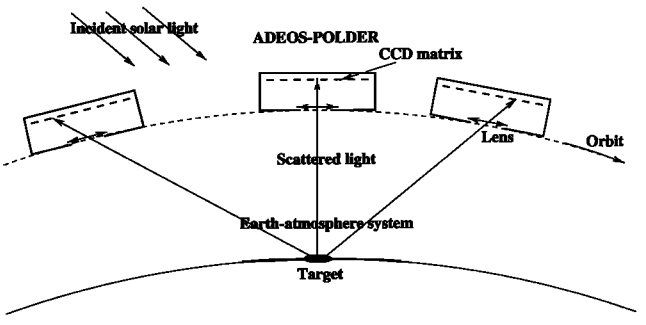

Figure 8. Viewing geometry of ADEOS-POLDER.

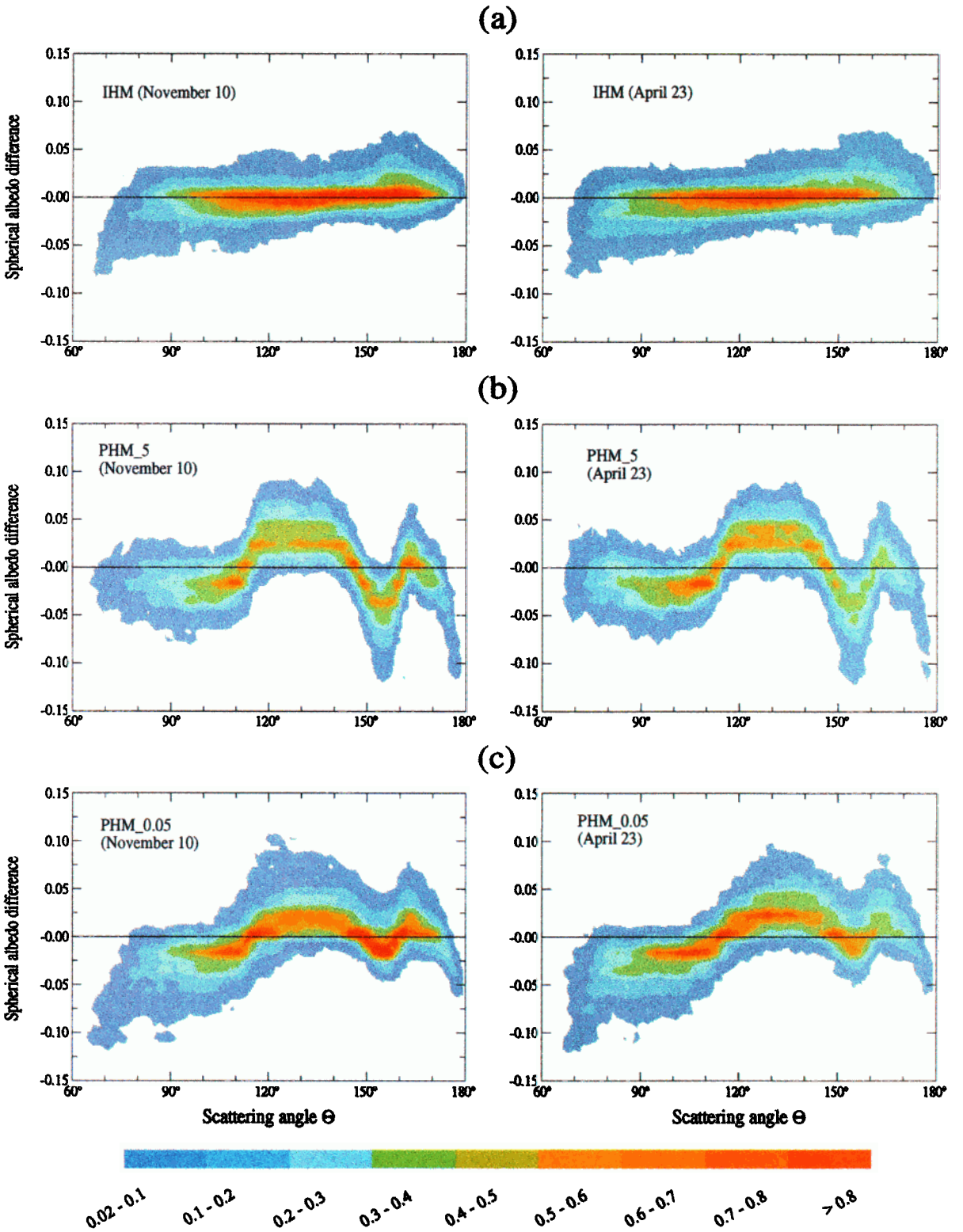

Plate 1. Difference between the directional and the directionality-averaged cirrus cloud spherical albedo, for IHM, PHM_5, and $PHM_{0.05}$ models as a function of scattering angle. Results are presented for November 10, 1996 and April 23, 1997. The color scale represents the density of the measurements normalized to the maximum density.

are 0.018 and 0.017 for November and April data, respectively, while for PHM_5, the values are 0.033 and 0.031, and for $PHM_{0\,05}$, the values are 0.026 and 0.029. The consistency between the November case and the April case suggests that throughout the year and whatever the geographical place, ice clouds with optical thickness $\delta_c > 1$ have the same dominating shape or the same optical properties in their uppermost level.

For the IHM model, Figure 9 shows, for several ranges of ice

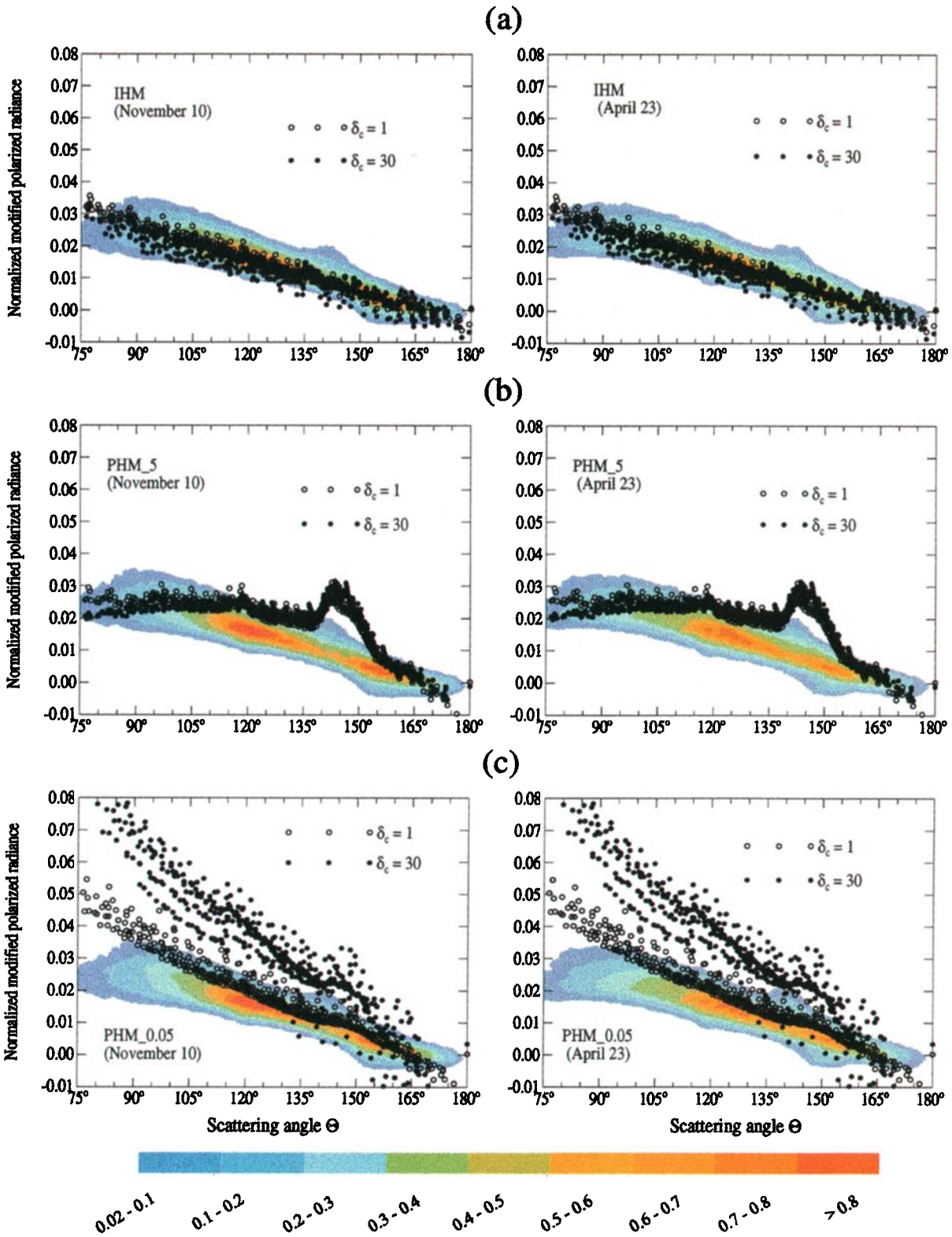

Plate 2. Comparison between ADEOS-POLDER measurements of normalized modified polarized radiance over ocean above 100% ice cloud cover, concerning the 14 orbits of November 10, 1996 and April 23, 1997, and simulations for IHM, PHM_5, and $PHM_{0.05}$ models. These three models present the same characteristics as for spherical albedo study. For the simulations, we have taken the ice cloud optical thickness equal to 1 and 30. The color scale represents the density of the measurements normalized to the maximum density (see text).

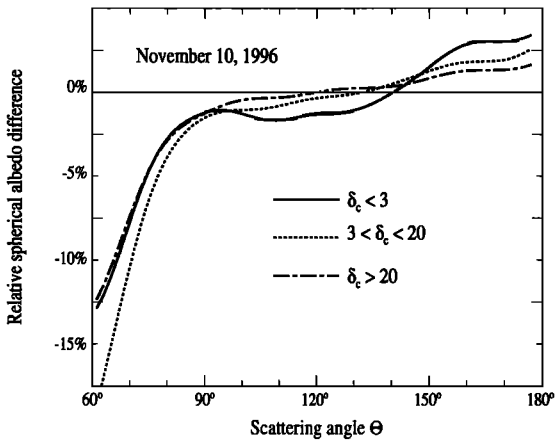

Figure 9. Effect of optical thickness on the spherical albedo difference as a function of scattering angle. The spherical albedo is derived from November 10 data by using the IHM model.

cloud optical thickness δ_c, the mean relative spherical albedo difference (s_{md}) as a function of scattering angle (Θ). Whatever the optical thickness δ_c may be, s_{md} has the same behavior with Θ. The departure from the zero line for scattering angles lower than 80° may be an indication of cloud heterogeneities which are not taken into account in our plane-parallel cloud layer model [*Jolivet*, 1998].

4.2. Polarized Radiances

Chepfer et al. [1998] showed that polarized reflectances are very sensitive to the shape of scatterers. Thus to further investigate the type of ice crystal shape in clouds, we must analyze the polarization properties of reflected light.

For a given scattering angle Θ, the polarized radiance is defined by

$$L_p = \text{sgn}\sqrt{Q^2 + U^2 + V^2}, \tag{9}$$

where $[Q, U, V]$ are the Stokes parameters. The scattering angle is obtained considering the incident solar direction $\vec{\Omega}_s$ relatively to the direction $\vec{\Omega}_v$ of the upward scattered light. These directions are characterized by the zenithal viewing and solar angles θ_v and θ_s, respectively, and the relative azimuth angle φ_r; sgn represents the sign (+1 or −1) of the polarized radiance (see Appendix A).

In the case of a large enough optical thickness (>2), and for the single-scattering approximation, the polarized radiance $L_p^{(1)}$ can be written as

$$L_p^{(1)} = \frac{E_s}{\pi}\frac{\varpi_0 Q_c(\Theta)\cos\theta_s}{4(\cos\theta_s + \cos\theta_v)}, \tag{10}$$

where E_s is the solar irradiance at the top of the atmosphere in the given channel, $Q_c(\Theta)$ is the polarized phase function for the scattering angle Θ, and ϖ_0 is the single-scattering albedo of the cloud particles. Then, the product of $L_p^{(1)}$ by $(\cos\theta_s + \cos\theta_v)/\cos\theta_s$ will be mainly governed by the scattering angle Θ, whatever the particular values of θ_s and θ_v [*Goloub et al.*, 1994]. Thus accounting for all orders of scattering, we define a normalized modified polarized radiance by

Table 2. Model of Atmosphere Used in the Adding-doubling Code

Adding-Doubling Code	
Stratosphere	molecules ($\delta_m = 0.01$)
Ice cloud	ice crystals ($1 < \delta_c < 50$)
Troposphere	molecules ($\delta_m = 0.03$) + maritime aerosols ($\delta_a = 0.1$)
Surface	sea $\rho_s = 6\%$

Optical thickness δ of each component is indicated.

$$L_{\text{nmp}}(\theta_v, \varphi_v; \theta_s, \varphi_s) = \frac{\pi L_p}{E_s}\frac{\cos\theta_s + \cos\theta_v}{\cos\theta_s}. \tag{11}$$

The polarized radiation field in the coupled ice cloud-atmosphere-ocean system is simulated by using the adding-doubling code developed by the Astronomy group of the University of Amsterdam [*De Haan et al.*, 1987]. The simulations are performed over ocean, by considering the atmospheric model reported in Table 2. We also use the standard maritime aerosol model following the *World Climate Research Program* (*WCRP*) [1986].

4.2.1. Comparison between modeling and measurements. We selected measurements of polarized radiances at 865 nm for 100% ice cloud cover pixels over ocean. Plate 2 presents, for November 10, 1996 (left panels), and April 23, 1997 (right panels), the 3-D histograms of normalized polarized radiance measurements L_{nmp} as a function of scattering angle Θ. These histograms, shown in color scale, are normalized to the maximum value. These measurements concern observations for all solar zenith angles and all azimuth angles found during the 14 orbits. For the study of L_{nmp} our criteria are not so restrictive as for the spherical albedo study (see section 4.1), this is why these plots account for measurements located all over the globe. Note that the thermodynamic cloud phase detection of the current POLDER algorithm only concerns ice clouds with optical thicknesses $\delta_c > 1$. Despite the large optical thickness variation of ice clouds (see Figure 7c), and the various geographical locations, measurements are remarkably gathered, with a behavior consisting of a general negative slope as a function of the scattering angle Θ. This means that whatever the detected ice cloud, ice crystals in the uppermost levels of ice clouds seem to have the same dominating shape or same optical properties.

For simulations we considered solar zenith angles θ_s within [20°, 50°] i.e., the higher solar zenith angle occurrence for all the observations of November 10 and April 23, and relative azimuth angles φ_r within [0°, 180°]. We varied the ice cloud optical thickness δ_c between 1 and 30, which is the main range of optical thicknesses seen from POLDER (see Figure 7c). Results of simulations performed by using IHM, PHM_5, and $\text{PHM}_{0.05}$ models are superimposed in Plate 2. As for the spherical albedo study (see section 4.1), these three models have the same characteristics. Simulations show that the $\text{PHM}_{0.05}$ model, whose aspect ratio was convenient for the EUCREX case study [*Chepfer et al.*, 1998], and the PHM_5 model with same aspect ratio as the IHM model used in the section 4.1

(study of spherical albedo), are inadequate for interpretation of these polarization measurements. Indeed, the PHM_5 model presents a very large bow for Θ within [140°, 150°], and the $PHM_{0.05}$ model is much more sensitive to the ice cloud optical thickness, considering the gathering of measurements. The best solution is given by the IHM model, for it fits adequately with POLDER measurements in the optical thickness range within 1 to 30.

4.2.2. More refined comparison between measurements and IHM model. In the previous section, we presented polarized reflectances where all met solar zenith angles were merged. In this section we analyze measurements and modeling as a function of solar zenith angle. To validate our model, it is interesting to study features of measurements of normalized modified polarized radiance from ADEOS-POLDER. There are related to different ice cloud optical thicknesses, with respect to different solar zenith angles. Figure 10 presents two scatterplots of L_{nmp} over ocean for 100% ice cloud cover, for November 10, 1996. The first one (Figure 10a) displays observations for θ_s within [20°, 21°] and all azimuth angles met during the 14 orbits, the second one (Figure 10b) lays out observations for θ_s within [51°, 52°]. We make the distinction between $\delta_c < 5$ and $\delta_c > 5$. One observes a slight decrease of L_{nmp} as δ_c increases for the small value of θ_s, while for the larger value of θ_s, the measured values of L_{nmp} are gathered whatever the optical thickness may be.

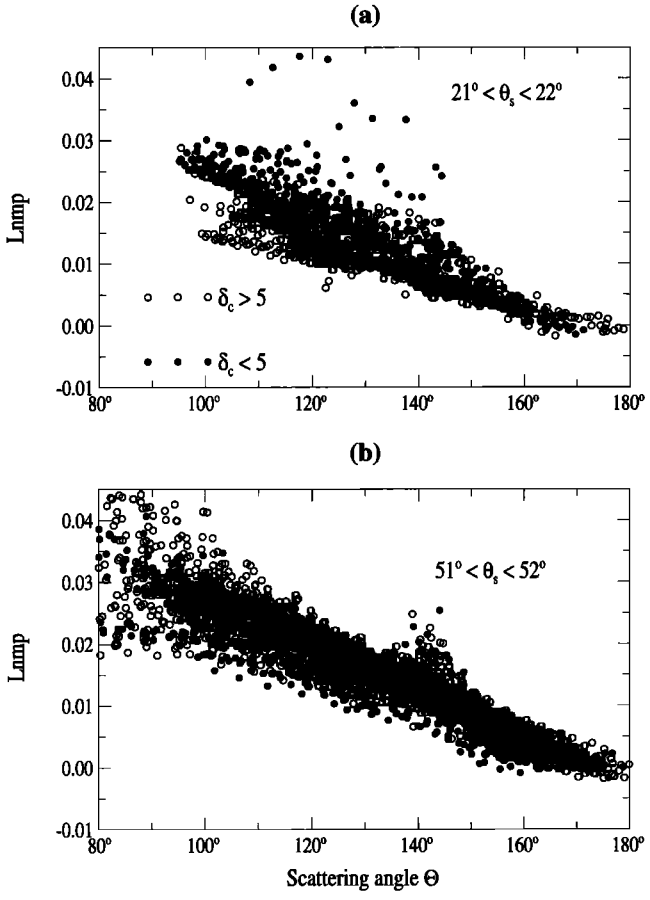

Figure 10. Scatterplots of measured normalized modified polarized radiance from ADEOS-POLDER as a function of scattering angle for θ_s within (a) [21°, 22°] and θ_s within (b) [51°, 52°].

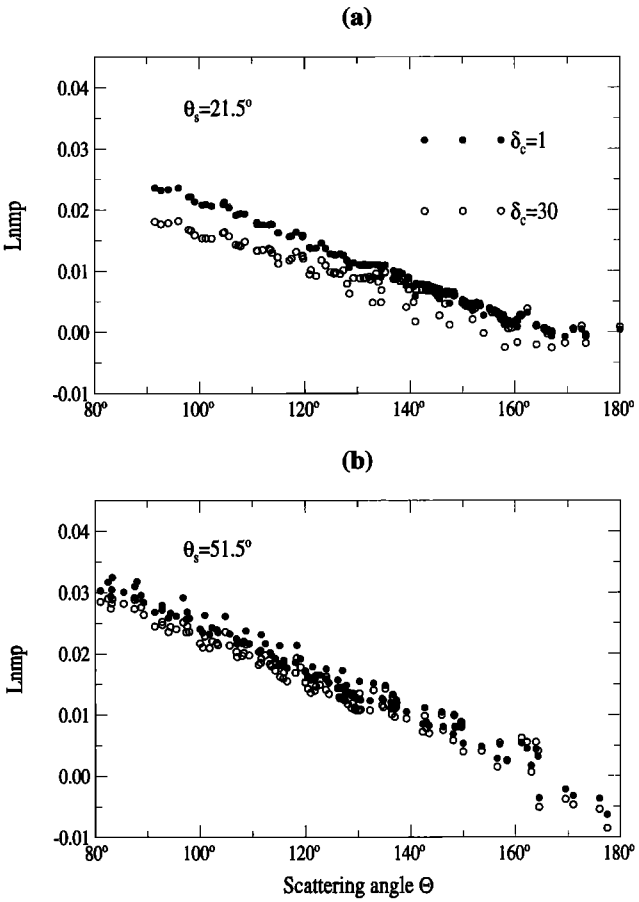

Figure 11. Scatterplots of simulated normalized modified polarized radiance as a function of scattering angle for (a) θ_s = 21.5°, and (b) θ_s = 51.5°. For these simulations the atmospheric model reported in Table 2 is used with IHMs.

Figure 11 shows scatterplots of normalized modified polarized radiance L_{nmp}, as a function of scattering angle Θ, simulated using the IHM model. Two ice cloud optical thicknesses (δ_c = 1 and δ_c = 30) are considered. In Figure 11a we present results obtained from a small value θ_s = 21.5° of the solar zenith angle, whereas in Figure 11b, we show results obtained from a larger value θ_s = 51.5°. The detailed characteristics displayed in the experimental data are confirmed by our calculations. For θ_s = 21.5°, L_{nmp} slightly decreases as δ_c increases, until it reaches a saturated value. On the other hand, for the larger value θ_s = 51.5°, the simulated L_{nmp} is hardly sensitive to δ_c. In this case, the optical thickness δ_c = 1 already corresponds to a saturated value of L_{nmp}. To sum up, the values of simulated L_{nmp} with respect to the ice cloud optical thickness, and with respect to solar zenith angle, are in good agreement with measurements. This feature confirms that this model is very suitable for interpreting polarization measurements.

For low values of solar zenith angle, the behavior of the polarized radiance (L_{nmp} slightly decreases when δ_c increases), could be qualified as strange, since the polarized radiance is expected to increase with δ_c. This behavior is due to molecular polarization effect below ice clouds. Indeed, for small ice cloud optical thicknesses and for small solar zenith angles, atmospheric molecules polarize more light than IHM particles for scattering angles within [60°, 110°]. For small solar zenith

angles, as δ_c increases, air molecules have less effects on the outgoing L_{nmp} which decreases until it reaches a limit value corresponding to lonely ice clouds. This limit value is more quickly reached for large solar zenith angles. Of course, the theoretical study of L_{nmp} without molecular scattering and whatever the solar zenith angle may be shows an increase of the polarized light with δ_c.

In the same way the behavior of the $\text{PHM}_{0.05}$ model with δ_c (Plate 2c) can be explained from its high degree of polarization, for scattering angles within [60°, 110°] [*Chepfer et al.*, 1998]. This degree of polarization is much more important than polarization due to atmospheric molecules. So, even with molecules, results of L_{nmp} show an increase with δ_c until reaching a saturated value. On the contrary, the degree of polarization of the PHM_5 model is of the same order of magnitude as the IHM model, which makes gathered results (Plate 2b) as for the IHM model.

5. Conclusion

The analysis presented in this paper shows the potentialities of the IHM model. Following in situ observations, the structural properties of this model are realistic and coherent. In particular, measurements performed with the PMS probe and the airborne polar nephelometer in ice clouds are in good agreement with calculations of differential scattering cross sections of IHM particles. Compared to the PHM model, the scattering matrix calculated from the IHM model allows to find very good results, both in terms of spherical albedo and in polarized reflectance derived from the ADEOS-POLDER measurements.

C.-Labonnote et al. [2000] thought that the study of polarization would be a constraint for the model to determine the shape of ice cloud particles. However, the present study, which is related to high values of ice cloud optical thickness, does not give the expected constraint to clearly discriminate the shape of the ice cloud scatters. Indeed, as inhomogeneities have depolarization effects, polarized radiance simulated from the IHM model is less sensitive to the shape, i.e., the aspect ratio of the hexagonal crystal, and the ice cloud optical thickness, than the one simulated from the PHM model. This fact seems to be in agreement with the densely gathered measurements, including all types of ice clouds. Anyway, several obvious particularities such as the presence of haloes on nephelometer measurements, and the general negative slope of measured L_{nmp} with the scattering angle, allowed us to think that the IHM is a good tool to modelize ice cloud particles, in terms of spherical albedo as well as in terms of polarized radiances. For a global study, this model seems to be well adapted to simulate the radiative properties of ice clouds.

Smoothing of scattering matrix elements may also result from averaging different particle habits, for example by adding medium-sized hexagons with different shapes like plates and columns, small quasi-spheres, and large irregular particles. In the near future this possibility will be explored. A next step of this study would consist in analyzing the POLDER data variability in terms of dominating shapes of cirrus ice crystals, for localized ice clouds with small optical thicknesses (semitransparent cirrus clouds). This future study will be implemented in the frame of the Pathfinder Instrument for Cloud and Aerosol Spaceborne Observations/Climatologie Etendue des Nuages et des Aerosols (PICASSO/CENA) mission [*Winker*, 1999]. Moreover, as the light absorption is no more negligible in the near infrared, it will be interesting to extend this study to the near-infrared wavelengths in order to determine the size of ice crystals and to confirm the validity of the IHM model over a large range of the spectrum.

Appendix A: Sign of Polarized Radiance

POLDER measurements are expressed with respect to the CCD matrix axes system $(\vec{u}_r, \vec{u}_l)$ (Figure A1), where $\vec{u}_l$ belongs to the meridian plane containing the viewing direction $\vec{\Omega}_v$. In this axes system, the direction $\vec{n}$ perpendicular to the scattering plane $(\vec{\Omega}_v, \vec{\Omega}_s)$ is characterized by the angle ψ and is expressed by

$$\vec{n} = \sin\psi\,\vec{u}_l + \cos\psi\,\vec{u}_r.$$

The direction $\vec{P}$ of polarization, characterized by the angle $\chi = \frac{1}{2}\arctan U/Q$, where U and Q are Stokes parameters of the scattered light, is defined by

$$\vec{P} = \cos\chi\,\vec{u}_l + \sin\chi\,\vec{u}_r.$$

The four unit vectors $\vec{u}_r, \vec{u}_l, \vec{P}$, and $\vec{n}$ are located at the same plane perpendicular to the viewing direction $\vec{\Omega}_v$.

In the reference frame $(\vec{i}, \vec{j}, \vec{k})$ the unit vectors ur, ul, and the direction $\vec{n}$ are given, respectively, by

$$\vec{u}_r = \begin{pmatrix} \sin\varphi_r \\ \cos\varphi_r \\ 0 \end{pmatrix}, \qquad \vec{u}_l = \begin{pmatrix} \cos\varphi_r\cos\theta_v \\ -\sin\varphi_r\cos\theta_v \\ \sin\theta_v \end{pmatrix},$$

$$\vec{n} = \begin{pmatrix} \cos\theta_s\sin\theta_v\sin\varphi_r \\ \cos\theta_s\sin\theta_v\cos\varphi_r + \sin\theta_s\cos\theta_v \\ -\sin\theta_s\sin\theta_v\sin\varphi_r \end{pmatrix}.$$

From identification the angle ψ is easily obtain by

$$\begin{cases} \sin\psi = -\sin\theta_s\sin\varphi_r \\ \cos\psi = \cos\theta_s\sin\theta_v + \sin\theta_s\cos\theta_v\cos\varphi_r \end{cases}$$

The sign sgn of the polarized radiance is given by the angle ξ derived from the scalar product $\cos\xi = \vec{n}.\vec{P} = \sin\psi\cos\chi + \cos\psi\sin\chi$. If ξ is within $[0, +\pi/4]$ or $[3\pi/4, \pi]$, then sgn = +1, else sgn = −1.

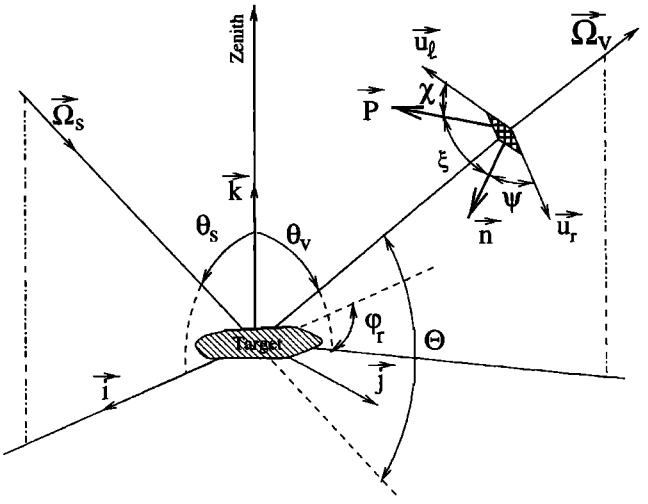

Figure A1. Viewing geometry of the polarized light measured by POLDER.

Acknowledgments. This work was funded by CNES and the Région Nord-Pas-de-Calais. Marie Doutriaux-Boucher was supported by a post doctoral grant from CNES. CIRRUS'98 experiment was supported by DGA/DSP/STTC. The authors are grateful to J. Hovenier and J. de Haan who gave the opportunity to use the adding-doubling code. Thanks are also due to M. Tavet for correcting the English text and to the three referees for their constructive remarks and comments.

References

Buriez, J. C., C. Vanbauce, F. Parol, P. Goloub, M. Herman, B. Bonnel, Y. Fouquart, P. Couvert, and G. Sèze, Cloud detection and derivation of cloud properties from POLDER, *Int. J. Remote Sens.*, *18*, 2785–2813, 1997.

Cai, Q., and K. N. Liou, Polarized light scattering by hexagonal ice crystal: Theory, *Appl. Opt.*, *21*, 3569–3580, 1982.

Chepfer, H., G. Brogniez, and Y. Fouquart, Cirrus clouds' microphysical properties deduced from POLDER observations, *J. Quant. Spectrosc. Radiat. Transfer*, *60*(3), 375–390, 1998.

Chepfer, H., G. Brogniez, L. Sauvage, P. H. Flamant, V. Trouillet, and J. Pelon, Remote sensing of cirrus radiative parameters during EUCREX'94: Case of 17 April 1994, part II, Microphysical models, *Mon. Weather Rev.*, *127*, 504–518, 1999.

C.-Labonnote, L., G. Brogniez, M. Doutriaux-Boucher, J.-C. Buriez, J. F. Gayet, and H. Chepfer, Modeling of light in cirrus clouds with inhomogeneous hexagonal monocrystals: Comparison with in-situ and ADEOS-POLDER measurements, *Geophys. Res. Lett.*, *27*(1), 113–116, 2000.

Crépel, O., J. F. Gayet, J. F. Fournol, and S. Oshchepkov, A new airborne polar nephelometer for the measurements of optical and microphysical cloud properties, part II, Preliminary tests, *Ann. Geophys.*, *15*, 460–470, 1997.

De Haan, J. F., P. B. Bosma, and J. W. Hovenier, The adding method for multiple scattering calculations of polarized light, *Astron. Astrophys.*, *183*, 371–391, 1987.

Deschamps, P. Y., F. M. Bréon, M. Leroy, A. Podaire, A. Bricaud, J. C. Buriez, and G. Sèze, The POLDER mission: Instrument characteristics and scientific objectives, *IEEE Trans. Geosci. Remote Sens.*, *32*, 598–615, 1994.

Doutriaux-Boucher, M., J.-C. Buriez, G. Brogniez, L. C.-Labonnote, and A. J. Baran, Sensitivity of retrieved POLDER directional cloud optical thickness to various ice particles models, *Geophys. Res. Lett.*, *27*(1), 109–112, 2000.

Durand, G., J. F. Gayet, L. Kaës, and P. Matharan, Airborne infrared and microphysical measurements on cirrus clouds, paper presented at the Conference on Satellite Remote Sensing of Clouds and Atmosphere, European Symposium on Remote Sensing, Barcelona, Spain, 21–25 September, 1998.

Gayet, J.-F., G. Febvre, G. Brogniez, H. Chepfer, W. Renger, and P. Wendling, Microphysical and optical properties of cirrus and contrails: Cloud field study on 13 October 1989, *J. Atmos. Sci.*, *53*, 126–138, 1996.

Gayet, J. F., O. Crépel, J. F. Fournol, and S. Oshchepkov, A new airborne polar nephelometer for the measurements of optical and microphysical cloud properties, part I, Theoretical design, *Ann. Geophys.*, *15*, 451–459, 1997.

Gayet, J. F., F. Auriol, S. Oshchepkov, F. Schroder, C. Duroure, G. Febvre, J.-F. Fournol, O. Crépel, P. Personne, and D. Daugeron, In situ measurements of the scattering phase function of stratocumulus, contrails and cirrus, *Geophys. Res. Lett.*, *25*(7), 971–974, 1998.

Girasole, T., H. Bultynck, G. Gouesbet, G. Gréhan, F. Le Meur, J. N. Le Toulousan, J. Mroczka, K. F. Ren, C. Rozé, and D. Wysoczanski, Cylindrical fibre orientation analysis by light scattering, part 1, Numerical aspects, *Part. Syst. Charact.*, *14*, 163–174, 1997.

Goloub, P., J. L. Deuzé, M. Herman, and Y. Fouquart, Analysis of the POLDER polarization measurements performed over cloud covers, *IEEE Trans. Geosci. Remote Sens.*, *32*, 78–88, 1994.

Hallett, J., Cirrus ice crystals nucleation and growth, in 74th AMS Annual Meeting, Am. Meteorol. Soc., Boston, Mass., 1994.

Heymsfield, A. J., K. M. Miller, and J. D. Spinhirne, The 27–28 October 1986 FIRE IFO case study: Cloud microstructure, *Mon. Weather Rev.*, *118*, 2313–2328, 1990.

Jolivet, D., Etude de l'influence de l'hétérogénéité des nuages sur le rayonnement solaire réfléchi vers l'espace, thèse d'université, 115 pp., Univ. des Sci. et Technol. de Lille, Lille, France, 1998.

Knap, W. H., M. Hess, P. Stammes, R. B. A. Koelemeijer, and P. D. Watts, Cirrus optical thickness and crystal size retrieval from ATSR-2 data using phase function of imperfect hexagonal ice crystals, *J. Geophys. Res.*, *104*, 31,721–31,730, 1999.

Lacis, A. A., and M. I. Mishchenko, Climate forcing, climate sensitivity, and climate response: A radiative modeling perspective on atmospheric aerosols, in *Aerosol Forcing of Climate*, edited by R. J. Charlson and J. Heistzenberg, pp. 11–42, John Wiley, New York, 1995.

Liou, K. N., Influence of cirrus clouds on weather and climate processes: A global perspective, *Mon. Weather Rev.*, *114*, 1167–1199, 1986.

Macke, A., J. Mueller, and E. Raschke, Single scattering properties of atmospheric ice crystals, *J. Atmos. Sci.*, *53*, 2813–2825, 1996a.

Macke, A., M. I. Mishchenko, and B. Cairns, The influence of light scattering by large ice particles, *J. Geophys. Res.*, *101*, 23,311–23,316, 1996b.

Miloshevich, L. M., and A. J. Heymsfield, A balloon-borne continuous cloud particle replicator for measuring vertical profiles of cloud microphysical properties: Instrument design, performance, and collection efficiency analysis, *J. Atmos. Oceanic Technol.*, *14*, 753–768, 1997.

Mischenko, M. I., and J. W. Hovenier, Depolarization of light backscattered by randomly oriented nonspherical particles, *Opt. Lett.*, *20*, 1356–1358, 1995.

Mischenko, M. I., and A. Macke, Asymmetry parameters of the phase function for isolated and densely packed spherical particles with multiple internal inclusions in the geometric optics limit, *J. Quant. Spectrosc. Radiat. Transfer*, *57*, 767–794, 1997.

Mishchenko, M. I., D. W. Mackowski, and L. D. Travis, Scattering of light by biospheres with touching and separated components, *Appl. Opt.*, *34*, 4589–4599, 1995.

Muinonen, K., Scattering of light by crystals: A modified Kirchhof approximation, *Appl. Opt.*, *28*, 3044–3050, 1989.

Noone, K. B., K. J. Noone, J. Heintzenberg, J. Ström, and J. A. Ogren, In situ observations of cirrus cloud microphysical properties using the Counterflow Virtual Impactor, *J. Atmos. Oceanic Technol.*, *10*, 294–303, 1993.

Parol, F., J. C. Buriez, C. Vanbauce, P. Couvert, G. Sèze, P. Goloub, and S. Cheinet, First results of the POLDER "Earth Radiation Budget and Clouds" operational algorithm, *IEEE Int. Geosci. Remote Sens.*, *37*, 1597–1612, 1999.

Rozé, C., Diffusion multiple de la lumière, part 2, Calcul par une méthode de Monte Carlo, in *Habilitation à Diriger les Recherches*, Univ. de Rouen, Rouen, France, 1999.

Sauvage, L., H. Chepfer, V. Trouillet, P. H. Flamant, G. Brogniez, J. Pelon, and F. Albers, Remote sensing of cirrus radiative parameters during EUCREX'94: Case study of 17 April 1994, Part I, Observations, *Mon. Weather Rev.*, *127*, 486–503, 1999.

Stamnes, K., S.-C. Tsay, W. J. Wiscombe, and K. Jayaweera, Numerically stable algorithm for discrete-ordinate-method radiative transfer in multiple scattering and emitting layered media, *Appl. Opt.*, *27*(2), 502–509, 1988.

Stephens, G. L., S. C. Tsay, P. W. Stackhouse, and P. J. Flateau, The relevance of the microphysical and radiative properties of cirrus clouds to climate and climatic feedback, *J. Atmos. Sci.*, *47*, 1742–1753, 1990.

Strauss, B., R. Meerkoetter, B. Wissinger, P. Wendling, and M. Hess, On the regional climatic impact of contrails: Microphysical and radiative properties of contrails and cirrus, *Ann. Geophys.*, *15*, 1457–1467, 1997.

Takano, Y., and K. Jayaweera, Scattering phase matrix for hexagonal ice crystals computed from ray optics, *Appl. Opt.*, *24*, 3254–3263, 1985.

van de Hulst, H. C., *Light Scattering by Small Particles*, 470 pp., Dover, Mineola, New York, 1981.

Wendling, P., R. Wendling, and H. K. Weickmann, Scattering of solar radiation by hexagonal ice crystals, *Appl. Opt.*, *18*, 2663–2671, 1979.

Winker, D. M., PICASSO-CENA mission, paper presented at EOS/SPIE Sympopsium on Remote Sensing, Florence, Sept. 20–24, 1999.

World Climate Research Program (WCRP), A preliminary cloud standart atmosphere for radiation computation, *WCP-112 WMO*, 60 pp., Geneva, Switzerland, 1986.

Yang, P., and K. N. Liou, Single-scattering properties of complex ice crystals in terrestrial atmosphere, *Contrib. Atmos. Phys.*, *71*, 223–248, 1998.

G. Brogniez, J.-C. Buriez, and L. C.-Labonnote, M. Doutriaux-Boucher Laboratoire d'Optique Atmosphérique, Université des Sciences et Technologies de Lille, 59655 Villeneuve d'Ascq Cedex, France. (labon@loa.univ-lille1.fr)

J. F. Gayet, Laboratoire de Météorologie Physique, Université Blaise Pascal, 63177 Aubère Cedex, France.

A. Macke, Abteilung Maritime Meteorologie Institut für Meereskunde, Universität zu Kiel, Kiel, Germany.

(Received March 9, 2000; revised September 14, 2000; accepted September 20, 2000.)